DOI: 10.1002/((please add manuscript number))
Article type: Communication

Retrieving the co-assembly pathway of composite cellulose nanocrystal photonic films from their angular optical response

Bruno Frka-Petesic, Joel A. Kelly, Gianni Jacucci, Giulia Guidetti, Gen Kamita, Nathan P. Crossette, Wadood Y. Hamad, Mark J. MacLachlan and Silvia Vignolini**

Dr. B. Frka-Petesic, G. Jacucci, Dr. G. Guidetti, Dr. G. Kamita, N. P. Crossette, Dr. S. Vignolini
Melville Laboratory for Polymer Synthesis, Department of Chemistry, University of Cambridge, Lensfield Road, Cambridge CB2 1EW, United Kingdom
E-mails: B.F.-P.: bf284@cam.ac.uk, S.V.: sv319@cam.ac.uk

Dr. J. A. Kelly, Prof. M. J. MacLachlan
Department of Chemistry, University of British Columbia, 2036 Main Mall, Vancouver, BC, Canada, V6T 1Z1

Dr. W. Y. Hamad
Transformation and Interfaces Group, FPInnovations, 2665 East Mall, Vancouver, BC, Canada V6T 1Z4

Keywords: cellulose nanocrystals, colloidal self-assembly, cholesterics, photonic structures, drying dispersions.

Aqueous suspensions of cellulose nanocrystals (CNCs) are known to self-assemble into a chiral nematic liquid crystalline phase, leading to solid-state nanostructured colored films upon solvent evaporation, even in the presence of templating agents. The angular optical response of these structures, and therefore their visual appearance, is completely determined by the spatial arrangement of the CNCs when the drying suspension undergoes a transition from a flowing and liquid crystalline to a kinetically arrested state.

Here, we demonstrate how the angular response of the final film allows for retrieval of key physical properties and the chemical composition of the suspension at the onset of the kinetic arrest, thus capturing a snapshot of the past. To illustrate this methodology, we investigated a dynamically evolving sol-gel co-assembly process by various amounts of organosilica precursor addition, namely 1,2-bis(trimethoxysilyl)ethane (BTMSE). We were able to track

the influence of the organosilica condensation on the kinetic arrest and thus explain the angular response of the resulting films. Our *a posteriori* and *in situ* approach is general, it can be applied to a variety of additives in CNC-based films and it allows accessing key rheological information of the suspension without using any dedicated rheological technique.

Cellulose nanocrystals (CNCs) are sustainable and bio-sourced chiral nano-splinters capable of self-assembling into cholesteric photonic structures by slow drying of colloidal dispersions, offering a sustainable, cost-effective and scalable route to optical materials.[1–4] Over the past decade, substantial development of CNC-based films with additional functionalities arose from the successful co-assembly of CNCs with other species, e.g., polymers, surfactants, proteins or latexes. Generating hybrid films allowed the community to address the brittleness of pure CNC films but also to incorporate new functionalities (e.g., fluorescence, plasmonic response, etc.).[5–9] Interestingly, CNC self-assembly is also compatible with several sol-gel precursors such as tetramethyl orthosilicate (TMOS), tetraethyl orthosilicate (TEOS) and organosilica precursors allowing for the fabrication of mesoporous structures inheriting their characteristic chiral photonic properties.[10–13] The versatility of CNCs and their ability to accommodate these guests allowed for the development of a variety of applications, namely, structural pigments,[14] anti-counterfeit coatings,[15] swelling[16] or mechanochromic sensors,[17,18] as well as depolarizing[19] or broadband reflectors.[20] Importantly, the presence of non-volatile additives often alter significantly the optical properties of the produced films.[21] In presence of TMOS and related sol-gel precursors, a red-shift in the reflected wavelength is commonly reported and associated to a larger cholesteric pitch, p, but its effect on the orientation of its helical axis, **m**, remained relatively unexplored.

The self-assembled structure produced upon drying is strongly influenced by the kinetic arrest transition of CNCs that necessarily occurs at some point before a solid material is produced. Before the kinetic arrest transition, the suspension is able to relax and adjust its cholesteric pitch, p (defined as its full-turn periodicity), to the continuously increasing concentration upon solvent evaporation. Once the suspension is kinetically arrested, the pitch is expected to vary mostly as a result of volume decrease and macroscopic contraction along the helix axis, the latter being strongly affected by the cholesteric alignment, the sample

geometry and the boundary conditions.[22–25] This essential step allows for the production of solid-state CNC materials with very distinctive internal structure and corresponding optical properties.[23,26–29] Only few dedicated studies highlighted the importance of the kinetic arrest in self-assembled CNC systems,[21,22,30–32] and only few rheological approaches were followed to identify the concentration at which it occurs.[30] However, the nature of the interaction between CNCs can strongly affect it. Indeed, excessive ionic strength is known to trigger CNC aggregation and lead to a percolated gel.[30,33,34] Alternatively, very low ionic strength (<0.1 mM) can also cause long-range repulsion even at low volume fraction,[35] leading to an arrested "colloidal Wigner glass". This jammed state is characterized by the absence of long range order and the presence of a finite shear rigidity.[32,36–39] In these systems, electrostatic caging prevents individual particles from moving independently by hindering each other's motion without being directly in contact.

In this work, we investigate the angular optical response of composite organosilica/Cellulose nanocrystal (OS/CNC) films produced by combining 1,2-bis(trimethoxysilyl)ethane (BTMSE) and CNCs. Various amounts of 1,2-bis(trimethoxysilyl)ethane (BTMSE) were added to an aqueous CNC suspension and the resulting mixtures were cast into petri dishes. The solvent was left to evaporate while the BTMSE was also allowed to condense into organosilica (OS). The optical signature of the kinetic arrest present in the angular response of the dry films allows us to easily capture *a posteriori* the conditions when the suspension underwent kinetic arrest.[21–23,30,32,40] Such a newly discovered link is highly significant as it enables a better fundamental understanding of the drying kinetic of the colloidal systems, which is challenging to determine otherwise with dedicated rheological techniques.[30,41]

The initial mass ratio of BTMSE to CNC (m_{BTMSE}: m_{CNC}) allowed determination of the composition of the final films after the evaporation of water and the condensation of BTMSE into OS. This corresponds, if fully condensed, to a -CH_2CH_2- bridged polysilsesquioxane

network $(Si_2O_3C_2H_4)_n$. As we found no significant mismatch between the estimated mass of OS derived from BTMSE:CNC stoichiometry when assuming full condensation and the TGA analysis in a previous study, we have assumed for this work that full condensation occurred in all films.[42] The estimated volume fractions of OS and CNC in composite films, as well as the resulting optical indices,[42,43] are reported for convenience in **Table 1** and **Supporting Information**.

Polarized optical microscopy images of the films were observed in reflection and in bright field (**Figure 1**). Under normal incidence, the films reflect specific colors only in left circular polarization, as expected from their left-handed chiral nematic structure. As previously reported,[13] the image sequence shows a clear red-shift as more OS is incorporated into the composites. Such a spectral shift has been reported with several other additives and can be understood as a direct effect of the reduction of the vertical collapse of the cholesteric structure upon drying when part of the volatile solvent volume fraction is replaced by a non-volatile counterpart. To quantify the observed redshift as more OS is incorporated, reflection spectra were measured on a large surface area using a double-ended fiber **(Figure 1b)**, which allows for collection of the reflection in a narrow cone of angles along the specular reflection direction.

The angular optical response of the composite films was characterized by angular-resolved optical spectroscopy. In short, each sample is illuminated with white light at a fixed incident angle (θ_{in} = 30°) and the spectrum of the reflected light is then collected at various angles. The measured intensities are represented as a heat map vs collection angle, θ_{out}, and wavelength, λ, as exemplified in **Figure 2a**, while the schematic in **Figure 2b** defines the angles introduced. For each collection angle, the wavelength at the maximum intensity, λ_{peak}, is extracted (**Figure 2c**), from which several remarkable features can be highlighted. First, the addition of OS leads to a clear redshift of the optical response. Second, for all the samples, a

redshift of the reflected wavelength is observed in off-specular conditions (i.e., for $\theta_{in} \neq \theta_{out}$) with respect to specular ($\theta_{in} = \theta_{out}$). This is at first counter-intuitive, as a naive application of Bragg's law for a given pitch in the films instead predicts a *blue-shift*. Finally, this tendency to reflect longer wavelength in off-specular conditions decreases significantly as the OS content in the films increases.

These peculiar effects can be explained by the dependence of the pitch on the tilt of the domains. The recorded angular response can be further processed using Bragg's law, corrected by Snell's law at the air-film interface, as introduced by Fergason for low birefringence cholesterics:[44]

$$p(\beta) = \lambda_{peak}(\theta_{in}, \theta_{out})/[n_{ave} \cos\psi(\theta_{in}, \theta_{out})] \quad (1)$$

$$\psi(\theta_{in}, \theta_{out}) = \frac{1}{2}\sin^{-1}\left(\frac{\sin\theta_{out}}{n_{ave}}\right) + \frac{1}{2}\sin^{-1}\left(\frac{\sin\theta_{in}}{n_{ave}}\right) \quad (2)$$

$$\beta(\theta_{in}, \theta_{out}) = \frac{1}{2}\sin^{-1}\left(\frac{\sin\theta_{out}}{n_{ave}}\right) - \frac{1}{2}\sin^{-1}\left(\frac{\sin\theta_{in}}{n_{ave}}\right) \quad (3)$$

where θ_{in} and θ_{out} are the incident and outgoing angles of light, respectively, and n_{ave} is the average optical index of the films. Here we also introduce the local Bragg angle, ψ, and the local tilt, β, of a domain with respect to the vertical axis, both uniquely defined for given $(\theta_{in}, \theta_{out})$ conditions. From the data provided by angular-resolved optical spectroscopy, we were able to determine the underlying pitch p and its dependence with the cholesteric domain tilt β, as reported in **Figure 2d**.

As discussed in recent publications,[23,32] both the angular response and the pitch vs tilt dependence can be derived from the onset of kinetic arrest occurring in the suspension upon drying. As the kinetic arrest occurs, multiple cholesteric domains are "frozen" in rotation and position, each of them being characterized by a local tilt β_{ka} and a cholesteric pitch p_{ka}, where "ka" refers to the kinetic arrest. Upon further drying, the fixed horizontal boundaries of the dish and the free vertical interface with air lead together to a unidirectional compression of the liquid crystalline structure quantified by a scaling factor $0 < \alpha < 1$. As defined, a value of

$\alpha = 0.2$ corresponds to a five-fold compression, (i.e., by a factor $\alpha^{-1} = 5$). The resulting films contain cholesteric domains with different sets of tilts β and pitches p that can be expressed in terms of their initial local tilts β_{ka} and the initial pitch p_{ka} as:

$$p(\beta) = p_{\mathrm{ka}} \sqrt{\alpha^2 \cos^2 \beta + \sin^2 \beta} \quad (4)$$

$$\beta = \tan^{-1}[\alpha \ \tan \beta_{\mathrm{ka}}] \quad (5)$$

This mechanism is qualitatively illustrated in **Scheme 1**. According to this simple model, the tilt β of initially vertically or horizontally aligned domains does not change upon compression ($\beta = \beta_{\mathrm{ka}}$) and their associated pitches are respectively the most compressed (i.e., $p(0°) = \alpha\, p_{\mathrm{ka}}$) or not compressed at all (i.e., $p(90°) = p_{\mathrm{ka}}$).

The compression of the liquid crystalline structure, characterized by α, can be related to the volume loss occurring between the kinetic arrest and the final film. Since the pitch variation is proportional to the volume contraction, which is occurring predominantly along the vertical direction, the volume fraction $\Phi_{\mathrm{CNC}}^{\mathrm{ka}}$ at the kinetic arrest can be estimated as

$$\Phi_{\mathrm{CNC}}^{\mathrm{ka}} = \alpha\, \Phi_{\mathrm{CNC}}, \quad (6)$$

where Φ_{CNC} is the volume fraction of CNCs in the final film. In the absence of a non-volatile additive and neglecting the porosity of the CNC films, we can assume here $\Phi_{\mathrm{CNC}} = 1$ in the film and retrieve the expression $\Phi_{\mathrm{CNC}}^{\mathrm{ka}} = \alpha$, introduced in our previous work.[32] When additional OS is present in the film, equation (6) still holds, except that Φ_{CNC} is now evaluated from the mass ratio $m_{\mathrm{BTMSE}}{:}\, m_{\mathrm{CNC}}$ used to prepare the films and reported in Table 1 (details in Supporting Information).

From our knowledge of the films composition (after all relative mass fractions were converted into volume fractions, *cf.* Table 1) and using the data provided by angular-resolved optical spectroscopy, we were able to apply this model and extract two fitting parameters, α and $p(0°)$ (**Figure 3a,b**), or equivalently, α and p_{ka} (**Figure 3a,c**). From these values, which were extracted solely from optical analysis, we were able to recover key information about the

suspension at the kinetic arrest, such as the volume fraction, the pitch and the concentration of CNCs and additives (**Figure 3**, more details in **Table S1-2**).

To validate our approach, we also compared the pitches estimated by our optical analysis with direct SEM observations. According to eq. (4-5), the direct pitch measurement in SEM in vertical domains is expected to match $p(0) = \alpha\, p_{\mathrm{ka}}$ (**Figure 3b**), while for those tilted by 90° they should compare with $p(90°) = p_{\mathrm{ka}}$ (**Figure 3c** and **Figure S1**). While extremely tilted domains are rare, the measurements made on the few encountered occurrences (on the sample $m_{\mathrm{BTMSE}}{:}\, m_{\mathrm{CNC}}$ = 60:40) appeared in excellent agreement with the estimations from our optical analysis.

As more OS is incorporated, an overall increase of the pitch $p(0)$ is observed (**Figure 3b**). Intuitively, this can be easily understood as a direct consequence of the decrease of the vertical compression experienced by the suspension, since a fraction of the initial volatile solvent (in our case, water) has been replaced by the non-volatile OS, reducing the magnitude of the vertical compression. However, the presence of an additive could also interfere with the self-assembly and the chiral interactions between CNCs, either to enhance or reduce them.[21] Therefore, if the added BTMSE would not modify the twisting between CNCs, we could expect the final pitch $p(0)$ of vertical domains to simply increase as a direct proportion of the added volume fraction of incorporated OS

$$p(0°) = p_{\mathrm{CNC}}(0°)/\Phi_{\mathrm{CNC}}, \tag{7}$$

where $p_{\mathrm{CNC}}(0°)$ is the pitch of vertical domains in the pure CNC film, used here as a reference. This ideal, non-interacting case is represented with a gray dashed line in Figure 3b. The observed pitch values qualitatively follow a similar trend, with a small pitch drift to lower values that will be discussed later.

The estimated CNC concentration at the kinetic arrest, $\Phi_{\mathrm{CNC}}^{\mathrm{ka}}$, appears to increase with addition of BTMSE (**Figure 3d**) while the pitch at the kinetic arrest, p_{ka}, decreases, and these

two effects are amplified for larger $m_{\mathrm{BTMSE}}{:}\,m_{\mathrm{CNC}}$ ratios, i.e., initially weak for $\Phi_{\mathrm{OS}} \approx 30\%$ and becoming much stronger at $\Phi_{\mathrm{OS}} \approx 60\%$. These observations suggest that the addition of BTMSE postpones the kinetic arrest. This "fluidifying effect" can be surprising, since sol-gel OS precursors like BTMSE also solidify themselves. Understanding this phenomenon is essential as it strongly affects the angular response of the resulting films. Indeed, the increase of $\Phi_{\mathrm{CNC}}^{\mathrm{ka}}$ combined with the decrease of Φ_{CNC} in the dry film as more OS is incorporated greatly reduces the overall vertical compression, α^{-1}, of the cholesteric structure upon solvent evaporation (Figure 3a). The origin of this dramatic decrease of the vertical compression is better understood with **Figure 3f**, where the pitch evolution from the kinetic arrest to the dry film is shown as a function of Φ_{CNC} as more OS is incorporated. Since the anisotropic strain causes the red-shift of the off-specular response, it explains why films with more OS present less red-shift in off-specular conditions.

To capture the twisting behavior of CNCs in the arrested suspension state, it is informative to decouple it from their different Φ_{CNC} in the film or $\Phi_{\mathrm{CNC}}^{\mathrm{ka}}$ at their individual kinetic arrest transitions. Upon solvent evaporation, from the onset of the kinetic arrest till complete film collapse, the pitch of vertical domains decreases as $p\left(0, \Phi_{\mathrm{CNC}}^{\mathrm{susp}}\right) = p_{\mathrm{ka}}\Phi_{\mathrm{CNC}}^{\mathrm{ka}}/\Phi_{\mathrm{CNC}}^{\mathrm{susp}}$, thus as $\sim 1/\Phi_{\mathrm{CNC}}^{\mathrm{susp}}$, where $\Phi_{\mathrm{CNC}}^{\mathrm{susp}}$ is the volume fraction of CNC at any point in the arrested state. The term $p_{\mathrm{ka}}\Phi_{\mathrm{CNC}}^{\mathrm{ka}}$ is uniquely defined for each sample and allows for the visualization of a small pitch decrease induced by the presence of added BTMSE at *fixed* CNC concentration in the arrested suspension (**Figure 3e**). In other words, these observations indicate an increase of the twisting power of the CNCs in the suspension environment prior to kinetic arrest. Note that this conclusion assumed $\rho_{\mathrm{OS}} = 1.685$ g cm^{-3}, based on the work of Wang et al. for non-porous OS.[45] While it is arguable that the density of OS could vary slightly with experimental conditions and thus be in our case slightly different from Wang et al., our conclusion remains valid even for ρ_{OS} as high as 2.1 g cm^{-1}, which is a safe upper limit.

Significantly, the variations of p_{ka} (Figure 3c), $\Phi_{\mathrm{CNC}}^{\mathrm{ka}}$ (Figure 3d) and $p_{\mathrm{ka}}\Phi_{\mathrm{CNC}}^{\mathrm{ka}}$ (Figure 3e) all show an increasing rate of change upon BTMSE addition, indicating that all these effects become more pronounced as the BTMSE volume fraction is increased.

These variations may originate from a decrease of the repulsive electrostatic interactions, as it is known to occur when, e.g., small quantities of electrolyte are added to an aqueous CNC suspension of low ionic strength. Colloidal suspensions of strongly repulsive particles in a low ionic strength medium can undergo a glass transition when concentrated above a threshold concentration.[46,47] In such systems, the repulsion range is of the order of the Debye length, κ^{-1}, and inducing a small decrease of κ^{-1} can melt the colloidal glass and shift the glass transition to higher CNC concentrations. In suspensions, κ^{-1} scales as $\sqrt{\varepsilon_r/I}$, where ε_r is the dielectric constant and I is the ionic strength of the medium. It follows that a drop of κ^{-1} is easily introduced by small addition of electrolyte. Such drop explains the pitch reduction in CNC suspension upon electrolyte addition.[48,49] However, BTMSE is not a charged species and should not cause significant variation of I, even at concentrations up to 3 M (**Figure 3g**). An increase of I either from the introduction of small ionic contaminants or the generation of transient polyvalent charged sol-gel species could be considered, but this option is not consistent with the variation of the changes observed on p_{ka}, $\Phi_{\mathrm{CNC}}^{\mathrm{ka}}$ and $p_{\mathrm{ka}}\Phi_{\mathrm{CNC}}^{\mathrm{ka}}$ as more BTMSE is added: the dependence of κ^{-1} as $1/\sqrt{I}$ would favor an initial large effect that should weaken upon further BTMSE addition, while the inverse trend is observed (i.e., a weak effect that becomes much stronger as more BTMSE is added).

The decrease of κ^{-1} as a result of ε_r drop could be a more convincing explanation for these observations. While the addition of BTMSE in the aqueous CNC suspension is initially moderate (<10 wt%), the suspension at the kinetic arrest has lost enough water to make the concentration of BTMSE high enough to significantly affect ε_r as a co-solvent. Note, while we found no value for the dielectric constant of BTMSE, we can expect a very low dielectric

permittivity (<10) considering the absence of strong dipoles or highly polarizable groups in the molecule. The condensation of BTMSE also releases large quantities of methanol (MeOH) during the condensation process. At the point of kinetic arrest, we ignore what proportion of co-solvent is BTMSE or methanol and what fraction of methanol already evaporated. Nevertheless, assuming full condensation of BTMSE and no methanol evaporation at the kinetic arrest (assumptions noted **) provides an upper bound to estimate the volume fraction of methanol in the sample, $\Phi_{\mathrm{MeOH}^{**}}^{\mathrm{ka}}$, and more specifically in the solvent fraction, $\Phi_{\mathrm{MeOH}^{**}}^{\mathrm{ka,solv}}$ (**Figure 3h**, details in Supporting Information). This allows for the estimation of the dielectric constant ${\varepsilon_r}^{**,\mathrm{ka}}$ in the resulting solvent, and since the Debye length varies as $\sqrt{\varepsilon_r}$, we report $\sqrt{{\varepsilon_r}^{**,\mathrm{ka}}}$ in **Figure 3i**. Clearly, $\sqrt{{\varepsilon_r}^{**,\mathrm{ka}}}$ changes very little at small BTMSE:CNC ratios but it varies dramatically at larger ratios. The variation of ${\varepsilon_r}^{**,\mathrm{ka}}$ induced by adding the BTMSE is thus more likely what causes the observed variations of p_{ka}, $\Phi_{\mathrm{CNC}}^{\mathrm{ka}}$ and $p_{\mathrm{ka}}\Phi_{\mathrm{CNC}}^{\mathrm{ka}}$ reported in Figure 3. Note that a change of ε_r in the suspension can also affect the associated van der Waals interactions between CNCs and additionally modify how CNCs mutually interact at high concentration and their corresponding chiral nematic pitch in solution.[50].

Alternatively, the condensation of BTMSE into dynamically growing nanoclusters of OS can also be responsible for the decrease of p_{ka} and $p_{\mathrm{ka}}\Phi_{\mathrm{CNC}}^{\mathrm{ka}}$ via a depletion and fractionation effect, whereby a certain fraction of the OS nanoclusters would grow larger and get expelled from the cholesteric domains (into the space between tactoids) and induce a higher local concentration of CNCs in the cholesteric phase. Such fractionation is usually observed for much larger nanoparticles ($\gtrsim$ 50 nm) in biphasic CNC suspensions.[51–53] This could occur here because of the high volume fraction of OS nanoparticles and their dynamically evolving size distribution as the condensation progresses. A larger number of smaller tactoids could facilitate the pitch equilibration upon concentration and thus postpone the kinetic arrest, effectively increasing $\Phi_{\mathrm{CNC}}^{\mathrm{ka}}$. Importantly, this phenomenon does not depend

on the nature of the kinetic arrest, i.e., whether it evolves into an attractive gel or a repulsive glass. While the optical analysis of the final films in Figure 1a does not easily allow for a reliable estimation of an average "domain size" to compare between samples, the grain boundaries between domains appear much more pronounced as more OS is added, which could be due to local OS accumulation. Further work is required to validate the proposed scenarios.

To conclude, the angular optical properties of CNC-based photonic films are tightly related to the kinetic arrest transition upon solvent evaporation, and this relationship is important for two reasons. First, the angular optical response can be used to estimate the composition of the suspension undergoing kinetic arrest and this allows decoupling of the effects of any additional species on the self-assembly in a rapid and elegant way. We illustrated this by elucidating the variations of key parameters we introduced, such as p_{ka}, $\Phi_{\mathrm{CNC}}^{\mathrm{ka}}$ and $p_{\mathrm{ka}}\Phi_{\mathrm{CNC}}^{\mathrm{ka}}$, and we found indications that the addition of OS precursor (BTMSE) results in a postponing of the kinetic arrest and a slight reduction of the pitch in suspension *in its arrested state*. The cause could be either a drop of dielectric constant of the solvent with significant release of methanol (associated with a glass transition at the kinetic arrest), or a depletion and fractionation of part of the OS nanoclusters during the condensation. Second, the dependence of the kinetic arrest with additives is shown to control the angular optical response of these systems, through the parameters $p(0)$ and α (or as p_{ka} and α) and justifies paying attention on this transition for the production of CNC-based materials with well-defined photonic properties. Indeed, the angular optical response of the CNC films present a strong red-shift in their off-specular response that is dramatically reduced in the presence of OS. This contributes to reducing the angular dependency of the reflected wavelength (off-specular iridescence). Finally, while the outcomes of this work are directly relevant to the broad community studying CNC-based photonic films and their applications, the experimental simplicity of our approach and the robustness of their conclusions suggest it

could be employed as a model system to investigate the onset of kinetic arrest in self-assembling dispersions and its dependence with various experimental parameters.

Experimental Section

General: BTMSE (1,2-bis(trimethoxysilyl)ethane, Acros Organics) was used without further purification. The CNCs were supplied by FPInnovation. The procedure of their preparation is similar to a previous work and is detailed in Supporting Information.[18]

Preparation of OS/CNC composite films: OS/CNC composite films were prepared by first probe sonicating the CNC suspension, then adding BTMSE dropwise with continuous stirring at room temperature, using the ratios of BTMSE/CNC (cf. Table 1). Films were cast by pouring the mixtures into polystyrene Petri dishes and leaving to dry under ambient conditions (details in Supporting Information).

Sample characterization methods using *polarized optical microscopy* (POM), *spectroscopy*, *angular-resolved optical spectroscopy* with high dynamic range[23,54,55] and *scanning electron microscopy* (SEM) are detailed in Supporting information.

Supporting Information
Supporting Information is available from the Wiley Online Library or from the author. Additional data related to this publication is available free of charge at the University of Cambridge data repository (https://doi.org/10.17863/CAM.48013).

Acknowledgements

The authors thank Ahu Gümrah Parry for valuable discussions and Richard M. Parker for critical reading of the manuscript. S.V. acknowledges BBSRC David Phillips fellowship [BB/K014617/1], the EPSRC grants [EP/R511675/1, EP/N016920/1, EP/K503757/1], The Isaac Newton Trust Cambridge 1423(g) 76933, European Research Council [ERC-2014-STG H2020 639088, ERC-PoC-2017 790518]. G.G. acknowledges EPSRC [1525292]. M.J.M. thanks NSERC for a Discovery Grant. The authors declare no conflict of interest.

Received: ((will be filled in by the editorial staff))
Revised: ((will be filled in by the editorial staff))
Published online: ((will be filled in by the editorial staff))

References

[1] R. J. Moon, A. Martini, J. Nairn, J. Simonsen, J. Youngblood, *Chem. Soc. Rev.* **2011**, *40*, 3941.

[2] J. P. F. Lagerwall, C. Schütz, M. Salajkova, J. Noh, J. Hyun Park, G. Scalia, L. Bergström, *NPG Asia Mater.* **2014**, *6*, e80.

[3] R. M. Parker, G. Guidetti, C. A. Williams, T. Zhao, A. Narkevicius, S. Vignolini, B. Frka-Petesic, *Adv. Mater.* **2018**, *30*, 1704477.

[4] E. Kontturi, P. Laaksonen, M. B. Linder, A. H. Nonappa, A. H. Gröschel, O. J. Rojas, O. Ikkala, *Adv. Mater.* **2018**, *30*, 1703779.

[5] G. Guidetti, S. Atifi, S. Vignolini, W. Y. Hamad, *Adv. Mater.* **2016**, *28*, 10042.

[6] R. Bardet, N. Belgacem, J. Bras, *ACS Appl. Mater. Interfaces* **2015**, *7*, 4010.

[7] K. Yao, Q. Meng, V. Bulone, Q. Zhou, *Adv. Mater.* **2017**, *29*, 1701323.

[8] A. Lukach, H. Thérien-Aubin, A. Querejeta-Fernández, N. Pitch, G. Chauve, M. Méthot, J. Bouchard, E. Kumacheva, *Langmuir* **2015**, *31*, 5033.

[9] C. C. Y. Cheung, M. Giese, J. A. Kelly, W. Y. Hamad, M. J. MacLachlan, *ACS Macro Lett.* **2013**, *2*, 1016.

[10] J. A. Kelly, K. E. Shopsowitz, J. M. Ahn, W. Y. Hamad, M. J. MacLachlan, *Langmuir* **2012**, *28*, 17256.

[11] J. A. Kelly, M. Giese, K. E. Shopsowitz, W. Y. Hamad, M. J. MacLachlan, *Acc. Chem. Res.* **2014**, *47*, 1088.

[12] K. E. Shopsowitz, H. Qi, W. Y. Hamad, M. J. MacLachlan, *Nature* **2010**, *468*, 422.

[13] K. E. Shopsowitz, W. Y. Hamad, M. J. MacLachlan, *J. Am. Chem. Soc.* **2012**, *134*, 867.

[14] R. Bardet, F. Roussel, S. Coindeau, N. Belgacem, J. Bras, *Carbohydr. Polym.* **2015**, *122*, 367.

[15] Y. P. Zhang, V. P. Chodavarapu, A. G. Kirk, M. P. Andrews, *J. Nanophotonics* **2012**, *6*, 63516.

[16] J. A. Kelly, A. M. Shukaliak, C. C. Y. Cheung, K. E. Shopsowitz, W. Y. Hamad, M. J. MacLachlan, *Angew. Chemie Int. Ed.* **2013**, *52*, 8912.

[17] M. Giese, M. K. Khan, W. Y. Hamad, M. J. MacLachlan, *ACS Macro Lett.* **2013**, *2*, 818.

[18] K. E. Shopsowitz, J. A. Kelly, W. Y. Hamad, M. J. MacLachlan, *Adv. Funct. Mater.* **2014**, *24*, 327.

[19] T. Hiratani, W. Y. Hamad, M. J. MacLachlan, *Adv. Mater.* **2017**, *29*, 1606083.

[20] Y. Cao, W. Y. Hamad, M. J. MacLachlan, *Adv. Opt. Mater.* **2018**, *6*, 1800412.

[21] X. Mu, D. G. Gray, *Langmuir* **2014**, *30*, 9256.

[22] R. M. Parker, B. Frka-Petesic, G. Guidetti, G. Kamita, G. Consani, C. Abell, S. Vignolini, *ACS Nano* **2016**, *10*, 8443.

[23] B. Frka-Petesic, G. Guidetti, G. Kamita, S. Vignolini, *Adv. Mater.* **2017**, *29*, 1701469.

[24] Q. Chen, P. Liu, F. Nan, L. Zhou, J. Zhang, *Biomacromolecules* **2014**, *15*, 4343.

[25] V. Cherpak, V. F. Korolovych, R. Geryak, T. Turiv, D. Nepal, J. Kelly, T. J. Bunning,

O. D. Lavrentovich, W. T. Heller, V. V. Tsukruk, *Nano Lett.* **2018**, acs. nanolett.8b02522.

[26] M. Roman, D. G. Gray, *Langmuir* **2005**, *21*, 5555.

[27] M. Ličen, B. Majaron, J. Noh, C. Schütz, L. Bergström, J. Lagerwall, I. Drevenšek-Olenik, *Cellulose* **2016**, *23*, 3601.

[28] J. H. Park, J. Noh, C. Schütz, G. Salazar-Alvarez, G. Scalia, L. Bergström, J. P. F. Lagerwall, *ChemPhysChem* **2014**, *15*, 1477.

[29] T. H. Zhao, R. M. Parker, C. A. Williams, K. T. P. Lim, B. Frka-Petesic, S. Vignolini, *Adv. Funct. Mater.* **2018**, *29*, 1804531.

[30] C. Honorato-Rios, A. Kuhnhold, J. R. Bruckner, R. Dannert, T. Schilling, J. P. F. Lagerwall, *Front. Mater.* **2016**, *3*, 21.

[31] D. G. Gray, *Nanomaterials* **2016**, *6*, 213.

[32] B. Frka-Petesic, G. Kamita, G. Guidetti, S. Vignolini, *Phys. Rev. Mater.* **2019**, *3*, 045601.

[33] K. R. Peddireddy, I. Capron, T. Nicolai, L. Benyahia, *Biomacromolecules* **2016**, *17*, 3298.

[34] F. Cherhal, F. Cousin, I. Capron, *Langmuir* **2015**, *31*, 5596.

[35] J. Araki, S. Kuga, *Langmuir* **2001**, *17*, 4493.

[36] H. M. Lindsay, P. M. Chaikin, *J. Chem. Phys.* **1982**, *76*, 3774.

[37] H. Tanaka, J. Meunier, D. Bonn, *Phys. Rev. E - Stat. Nonlinear, Soft Matter Phys.* **2004**, *69*, 031404.

[38] H. Tanaka, S. Jabbari-Farouji, J. Meunier, D. Bonn, *Phys. Rev. E - Stat. Nonlinear, Soft Matter Phys.* **2005**, *71*, 021402.

[39] D. Bonn, H. Tanaka, G. Wegdam, H. Kellay, J. Meunier, *Europhys. Lett.* **2007**, *45*, 52.

[40] D. G. Gray, *Philos. Trans. R. Soc. A Math. Phys. Eng. Sci.* **2018**, *376*, 20170038.

[41] C. Honorato-Rios, C. Lehr, C. Schütz, R. Sanctuary, M. A. Osipov, J. Baller, J. P. F.

Lagerwall, *NPG Asia Mater.* **2018**, *10*, 455.

[42] W. Wang, D. Grozea, S. Kohli, D. D. Perovic, G. A. Ozin, *ACS Nano* **2011**, *5*, 1267.

[43] A. G. Dumanli, H. M. van der Kooij, G. Kamita, E. Reisner, J. J. Baumberg, U. Steiner, S. Vignolini, *ACS Appl. Mater. Interfaces* **2014**, *6*, 12302.

[44] J. L. Fergason, *Mol. Cryst.* **1966**, *1*, 293.

[45] A. M. M. Santos, W. L. Vasconcelos, *Mater. Res.* **1999**, *2*, 201.

[46] M. Schlesinger, W. Y. Hamad, M. J. MacLachlan, *Soft Matter* **2015**, *11*, 4686.

[47] E. Zaccarelli, *J. Phys. Cond. Mat.* **2007**, *19*, 323101.

[48] J.-F. Revol, D. L. Godbout, D. G. Gray, *J. pulp Pap. Sci.* **1998**, *24*, 146.

[49] X. M. Dong, T. Kimura, J.-F. Revol, D. G. Gray, *Langmuir* **1996**, *12*, 2076.

[50] J. R. Bruckner, A. Kuhnhold, C. Honorato-Rios, T. Schilling, J. P. F. Lagerwall, *Langmuir* **2016**, *32*, 9854.

[51] Y. Li, J. Jun-Yan Suen, E. Prince, E. M. Larin, A. Klinkova, H. Thérien-Aubin, S. Zhu, B. Yang, A. S. Helmy, O. D. Lavrentovich, E. Kumacheva, *Nat. Commun.* **2016**, *7*, 12520.

[52] Y. Li, E. Prince, S. Cho, A. Salari, Y. Mosaddeghian Golestani, O. D. Lavrentovich, E. Kumacheva, *Proc. Natl. Acad. Sci. U. S. A.* **2017**, *114*, 2137.

[53] P. Wang, W. Y. Hamad, M. J. MacLachlan, *Angew. Chemie Int. Ed.* **2018**, *57*, 3360.

[54] G. Kamita, B. Frka-Petesic, A. Allard, M. Dargaud, K. King, A. G. A. G. Dumanli, S. Vignolini, *Adv. Opt. Mater.* **2016**, *4*, 1950.

[55] D.-P. Song, G. Jacucci, F. Dundar, A. Naik, H.-F. Fei, S. Vignolini, J. J. Watkins, *Macromolecules* **2018**, *51*, 2395.

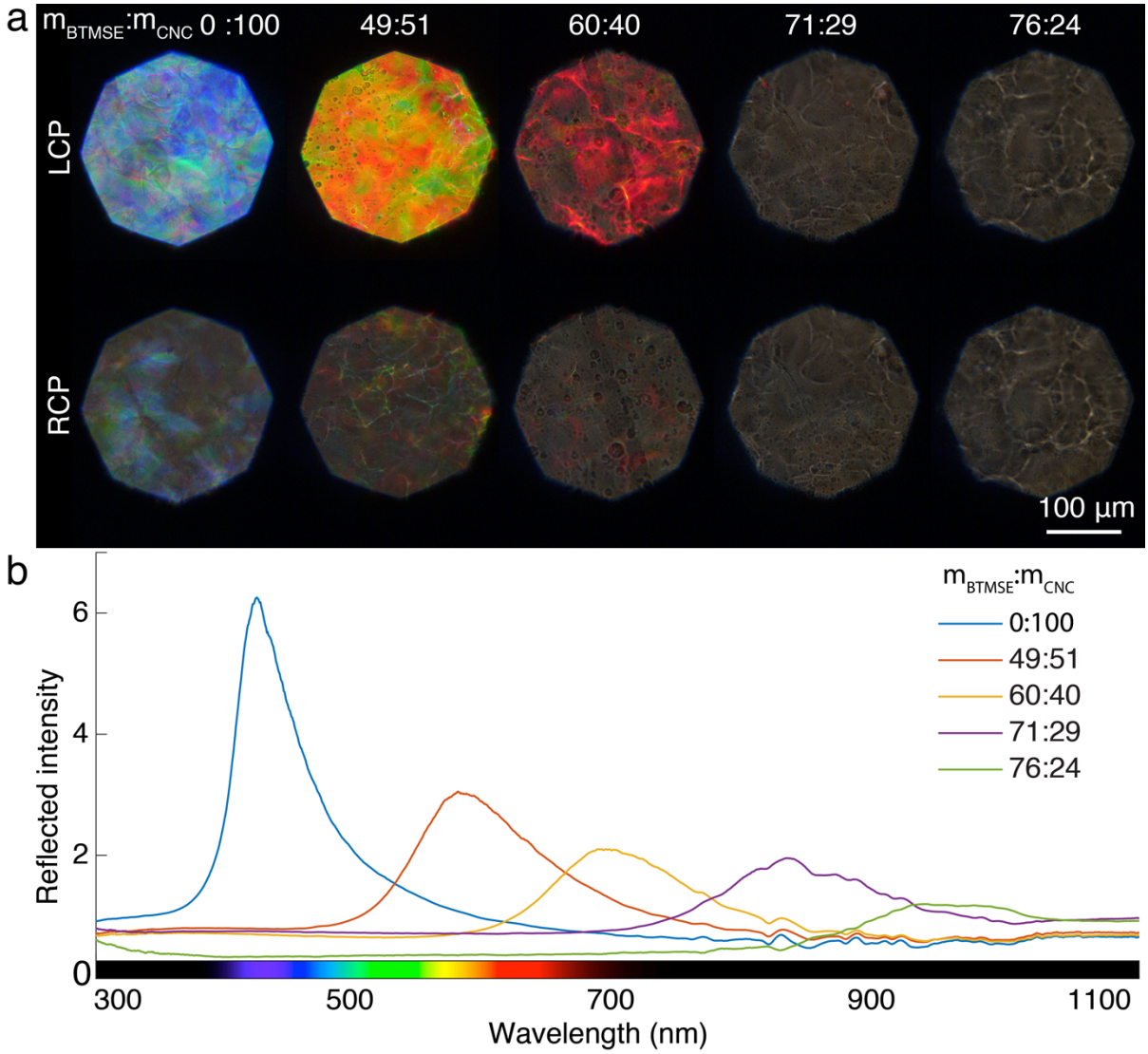

Figure 1. Optical characterization of the composite organosilica/cellulose nanocrystal (OS/CNC) films made with increasing BTMSE:CNC ratios. a) Polarized optical microscopy in reflection using respectively left- (LCP) and right-circular polarization (RCP) filters, showing a red-shift of the reflected light. b) Reflection spectra measured on the same samples using a double-ended fiber in normal incidence, normalized to a white diffuser.

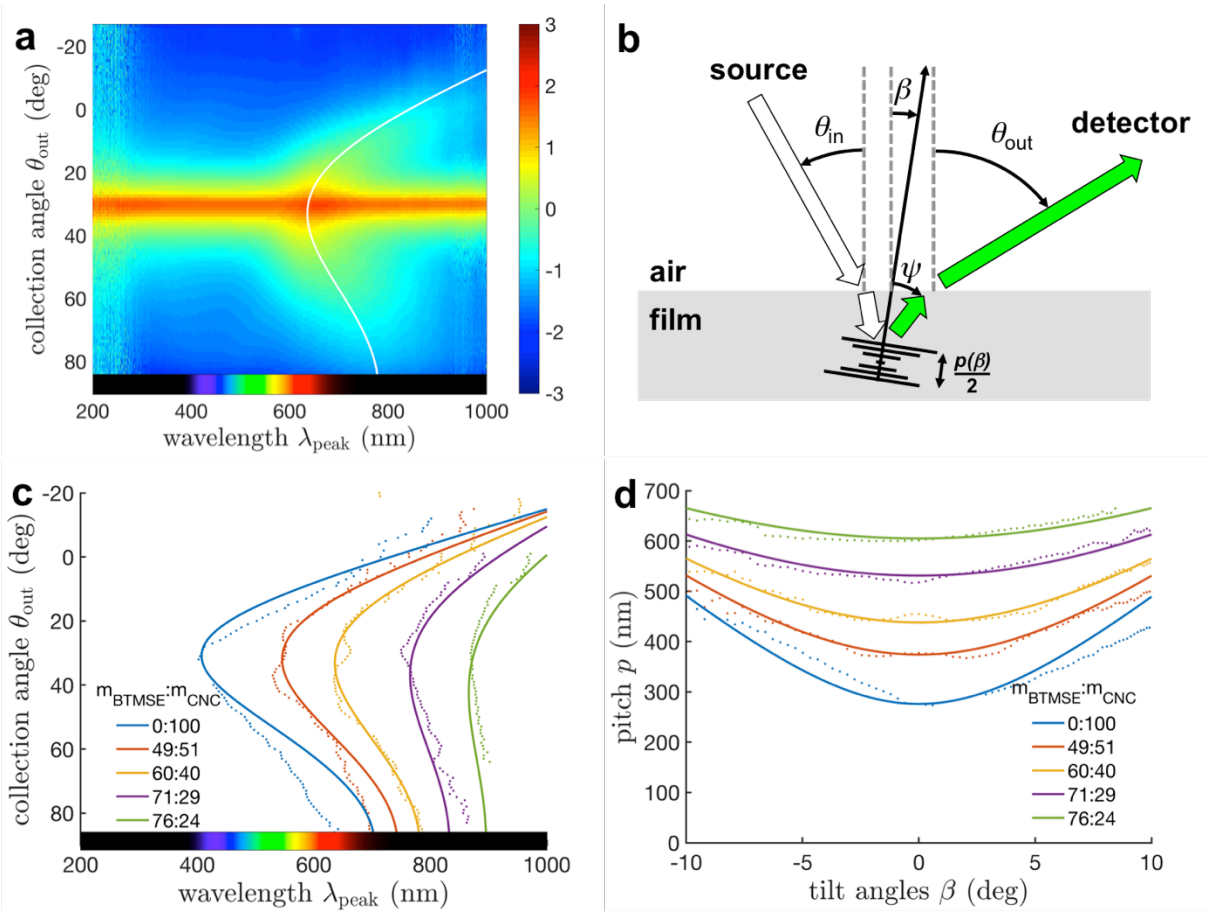

Figure 2. a) Angular-resolved optical spectroscopy of an OS/CNC composite film (m_{BTMSE}:m_{CNC} = 60:40) reporting the light intensity as a heatmap vs collection angles θ_{out} and wavelengths λ and a fit (solid line, using Equations 1-5 and θ_{in} = 30°). b) Schematic of the goniometer set-up and the angle definition. c) Peak wavelength λ_{peak} reflected at different θ_{out} (data in dots, fits in solid lines) and d) the corresponding pitches.

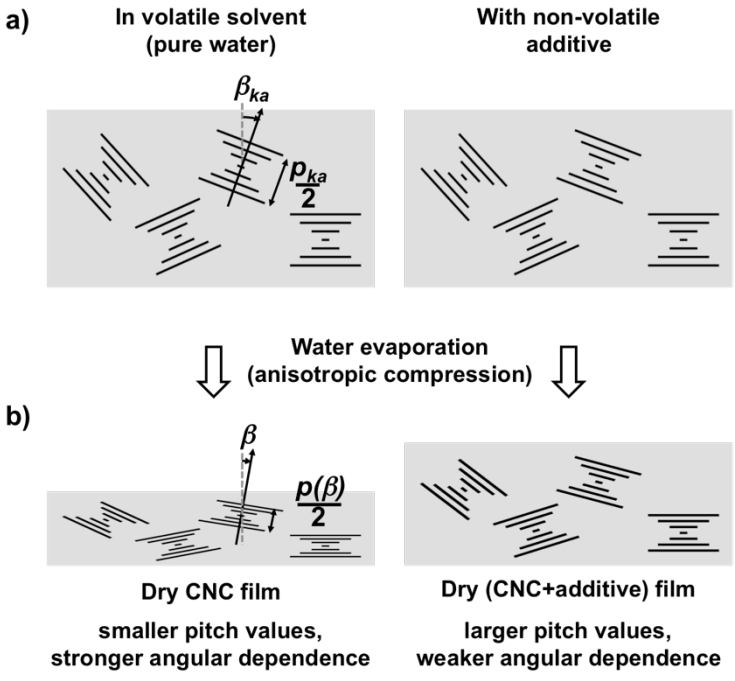

Scheme 1. Illustration of the vertical compression experienced by the cholesteric domains upon solvent compression, in the absence (left) or presence of a non-volatile additive (right), from a) the kinetic arrest transition until b) complete evaporation of the volatile fraction. The final pitch $p(\beta)$ retains information about the initial pitch p_{ka} and its compression ratio α, related to the suspension composition at the kinetic arrest.

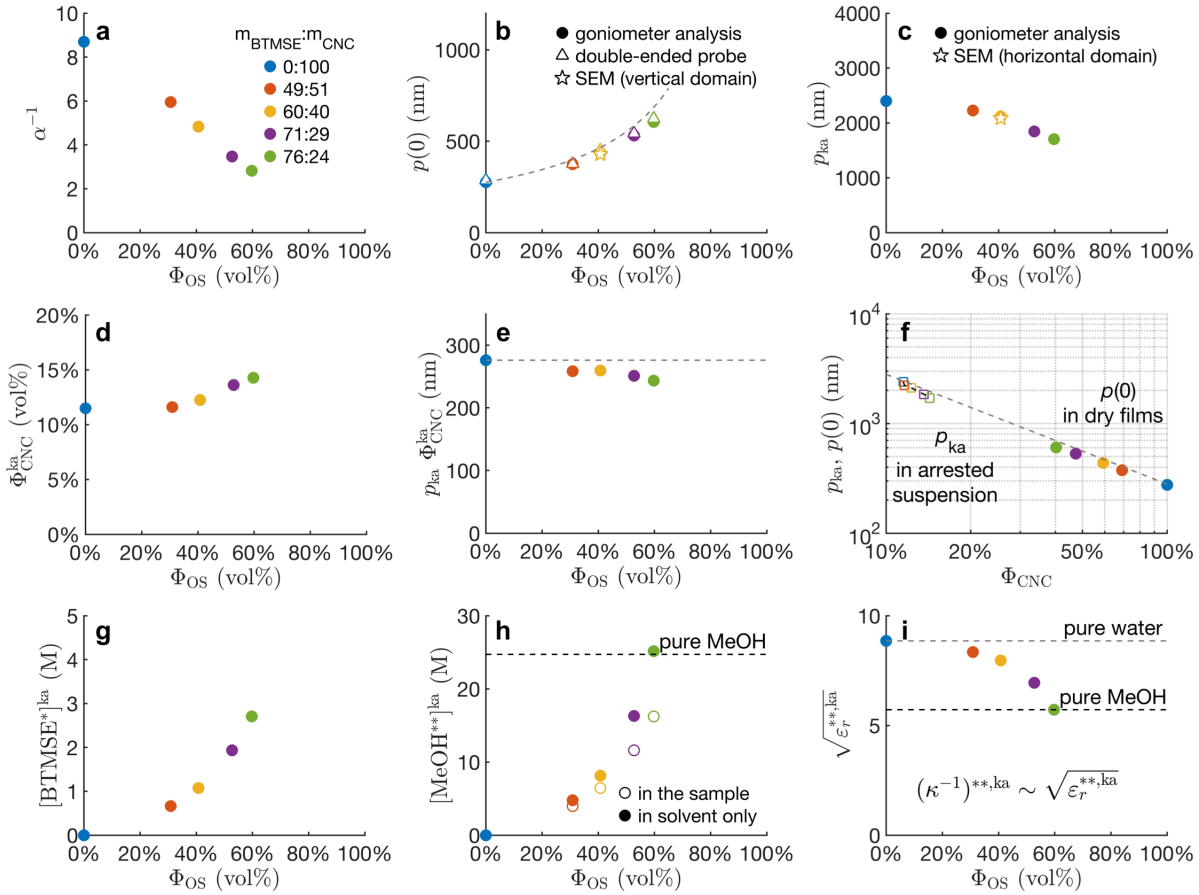

Figure 3. Summary of the information retrieved from the optical analysis of films for different m_{BTMSE}:m_{CNC}, and reported in function of volume fractions of OS (Φ_{OS}) or CNC (Φ_{CNC}). α^{-1}: vertical compression factor; $p(\beta)$: pitch of domains of tilt β in films; p_{ka}: pitch at the kinetic arrest, Φ_{CNC}^{ka}: volume fraction at kinetic arrest; $[BTMSE^*]^{ka}$: [BTMSE] at the kinetic arrest, assuming no condensation has yet occurred; $[MeOH^{**}]^{ka}$, $\varepsilon_r^{**,ka}$ and $(\kappa^{-1})^{**,ka}$: maximum [MeOH], dielectric constant and Debye length at the kinetic arrest, assuming all the BTMSE has condensed and no MeOH has evaporated yet. The gray dashed lines represent the ideal case for which BTMSE and water would have the same effect on the CNC pitch.

Table 1. Summary of the composite film composition.

m_{BTMSE}:m_{CNC} [wt/wt]	$[BTMSE]_{3wt\%}$ [M][a)]	c_{OS} [wt%]	c_{CNC} [wt%]	Φ_{OS} [vol%]	Φ_{CNC} [vol%]	n_{ave}
0:100	0.00	0	100	0.0	100.0	1.55(5)
49:51	0.11	32	68	30.9	69.1	1.54(1)
60:40	0.17	42	58	40.7	59.3	1.53(7)
71:29	0.27	54	46	52.7	47.3	1.53(1)
76:24	0.36	61	39	59.8	40.2	1.52(8)

[a)] $[BTMSE]_{3wt\%}$ corresponds to the initial [BTMSE] rescaled to a c_{CNC} = 3 wt% suspension.

The angular responses of photonic CNC-based films are investigated and related to the kinetic arrest transition occurring in the suspension upon solvent evaporation during the early stages of the film formation. We elucidate how addition of sol-gel organosilica precursor to the suspension alters the resulting angular response, through a delayed kinetic arrest and a reduced vertical collapse of the structure.

Cellulose nanocrystals, colloidal self-assembly, cholesterics, photonic structures, organosilica, nanotemplating, drying dispersions

B. Frka-Petesic,* J. A. Kelly, G. Jacucci, G. Guidetti, G. Kamita, N. P. Crossette, W. Y. Hamad, Mark J. MacLachlan and S. Vignolini*

Retrieving the co-assembly pathway of composite cellulose nanocrystal photonic films from their angular optical response

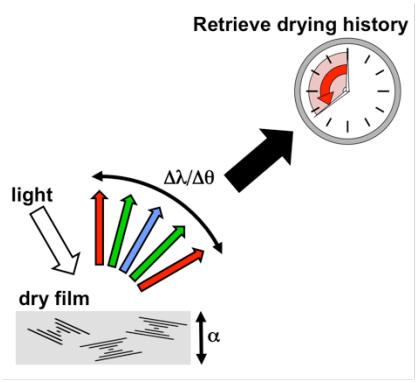

Supporting Information

Retrieving the co-assembly pathway of composite cellulose nanocrystal photonic films from their angular optical response

Bruno Frka-Petesic, Joel A. Kelly, Gianni Jacucci, Giulia Guidetti, Gen Kamita, Nathan P. Crossette, Wadood Y. Hamad, Mark J. MacLachlan and Silvia Vignolini**

1) Supporting tables and figures

Table S1. Summary of the main information deduced from the goniometer analysis of the film (Table S2 for complementary information).

$m_{\mathrm{BTMSE}}:m_{\mathrm{CNC}}$	$\lambda = n\,p(0)$	$p(0)$	p_{ka}	α	$\Phi^{\mathrm{ka}}_{\mathrm{CNC}}$	$c^{\mathrm{ka}}_{\mathrm{CNC}}$	$p_{\mathrm{ka}}\Phi^{\mathrm{ka}}_{\mathrm{CNC}}$
[wt/wt]	[nm]	[nm]	[µm]	[Ø]	[vol%]	[wt%]	[nm]
0:100	429	276	2.40	0.115	11.5	17.2	276
49:51	576	374	2.23	0.168	11.6	17.4	258
60:40	673	438	2.12	0.207	12.3	18.3	260
71:29	813	531	1.84	0.288	13.6	20.1	251
76:24	925	605	1.70	0.355	14.3	21.1	243

Table S2. Additional information deduced from the goniometer analysis.

$m_{\mathrm{BTMSE}}:m_{\mathrm{CNC}}$	$\Phi^{\mathrm{ka}}_{\mathrm{CNC}}$	$c^{\mathrm{ka}}_{\mathrm{CNC}}$	$\Phi^{\mathrm{ka}}_{\mathrm{BTMSE*}}$	$\Phi^{\mathrm{ka}}_{\mathrm{OS**}}$	$\Phi^{\mathrm{ka}}_{\mathrm{MeOH**}}$	$\Phi^{\mathrm{ka}}_{\mathrm{water**}}$	$[\mathrm{BTMSE^*}]^{\mathrm{ka}}$	$[\mathrm{MeOH^{**}}]^{\mathrm{ka}}$	$[\mathrm{MeOH^{**}}]^{\mathrm{ka,solv}}$	$\varepsilon_r{}^{**,\mathrm{ka}}$	$\sqrt{\varepsilon_r{}^{**,\mathrm{ka}}}$
[wt/wt]	[wt%	[wt%	[vol%]	[vol%]	[vol%]	[vol%]	[M][a)]	[M][a)]	[M][a)]	[Ø]	[Ø]
0:100	11.5	17.2	0.0	0.0	0.0	88.5	0.00	0.0	0.0	78.4	8.9
49:51	11.6	17.4	16.7	5.2	16.0	67.2	0.66	4.0	4.8	69.6	8.3
60:40	12.3	18.3	27.1	8.4	26.1	53.2	1.07	6.4	8.1	63.4	8.0
71:29	13.6	20.1	48.8	15.2	47.0	24.2	1.93	11.6	16.3	48.3	6.9
76:24	14.3	21.1	68.1	21.2	65.6[b)]	-1.1[b)]	2.70	16.2	25.2[b)]	32.7	5.7

[a)] $\Phi^{\mathrm{ka}}_{\mathrm{BTMSE*}}$ refers to the volume fraction of BTMSE at the kinetic arrest if no condensation has occurred, while $\Phi^{\mathrm{ka}}_{\mathrm{OS**}}$ in case of full condensation. $\Phi^{\mathrm{ka}}_{\mathrm{MeOH**}}$ is then the maximum released methanol volume fraction in the sample if no evaporation has occurred at the kinetic arrest, and $\Phi^{\mathrm{ka,solv}}_{\mathrm{MeOH**}}$ in the solvent only, and $\varepsilon_r{}^{**,\mathrm{ka}}$ is the corresponding relative permittivity of the methanol/water solvent only. [b)] Physically impossible values, indicating that some of the methanol must have evaporated.

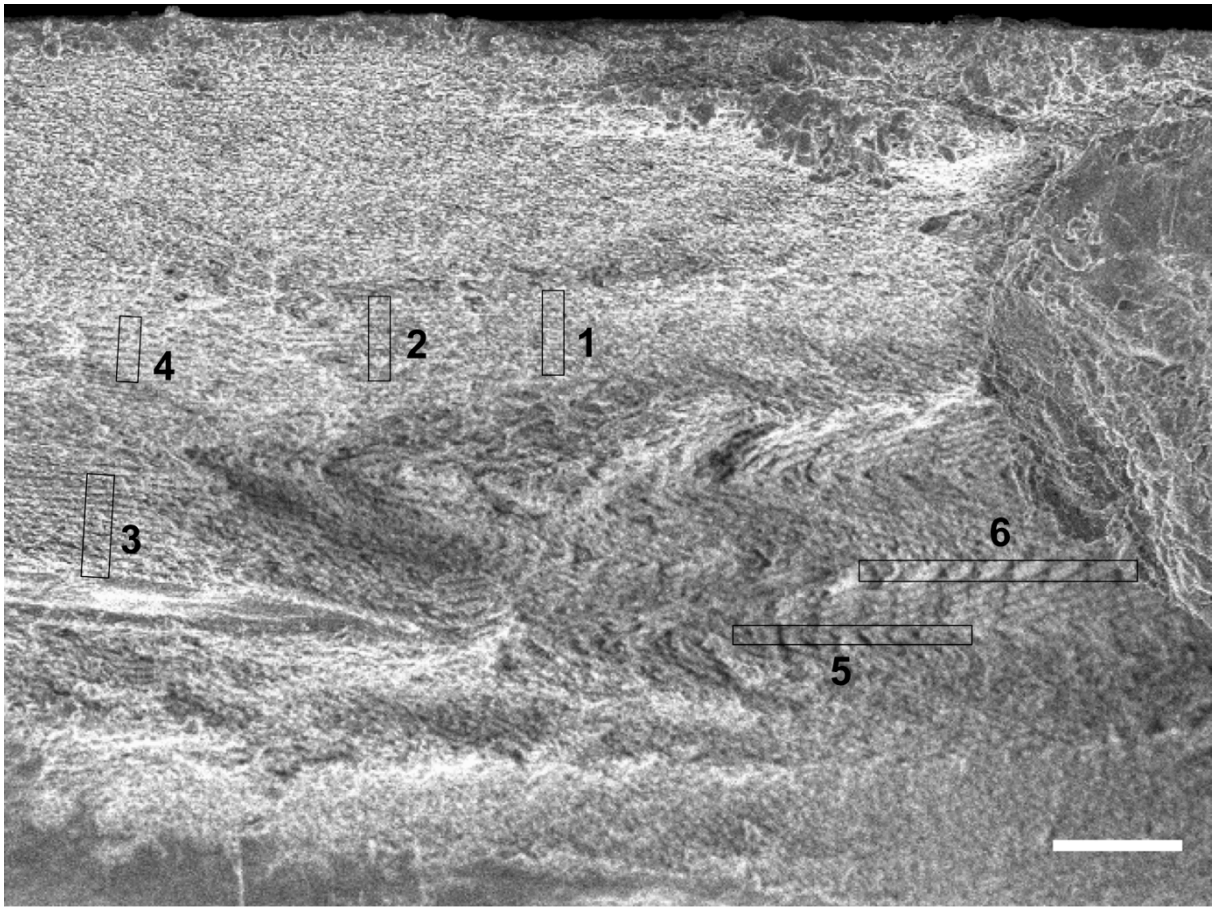

Figure S1. SEM image of the cross-section of a composite film (m_{BTMSE}: m_{CNC} = 60:40). The regions (1-6) were analyzed by profile plots (integrated over a width of 9 pixel) allowing for an estimation of the apparent pitch in the vertical and horizontal directions. This low magnification allows for seeing the surface of the film and compare with the domain tilt.

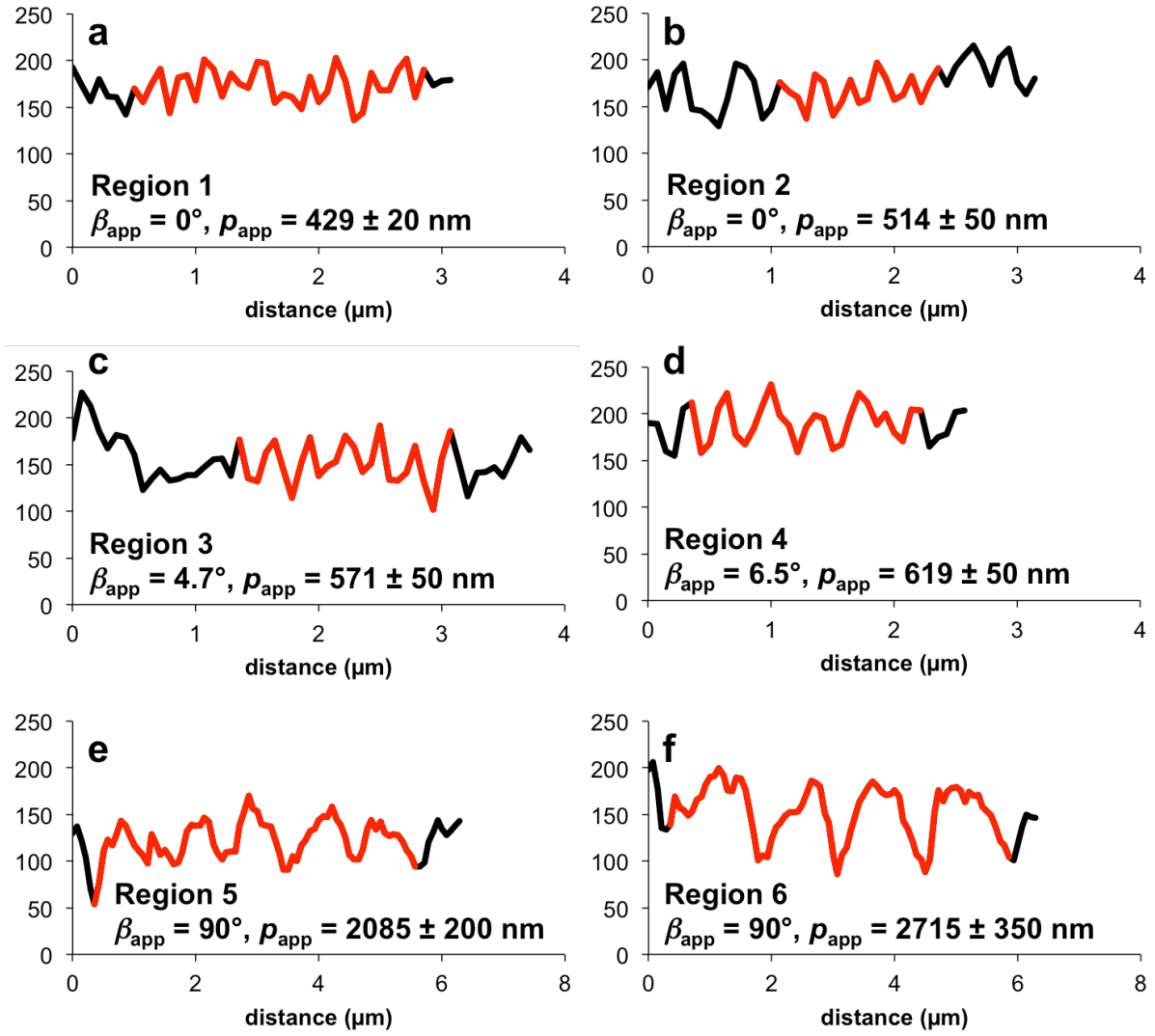

Figure S2. Gray scale intensity profile plots (in arbitrary unit), measured in the regions (1-6) of Figure S1 (sample m_{BTMSE}: m_{CNC} = 60:40), allowing for the determination of the apparent pitch p_{app} in the different directions, vertical and horizontal.

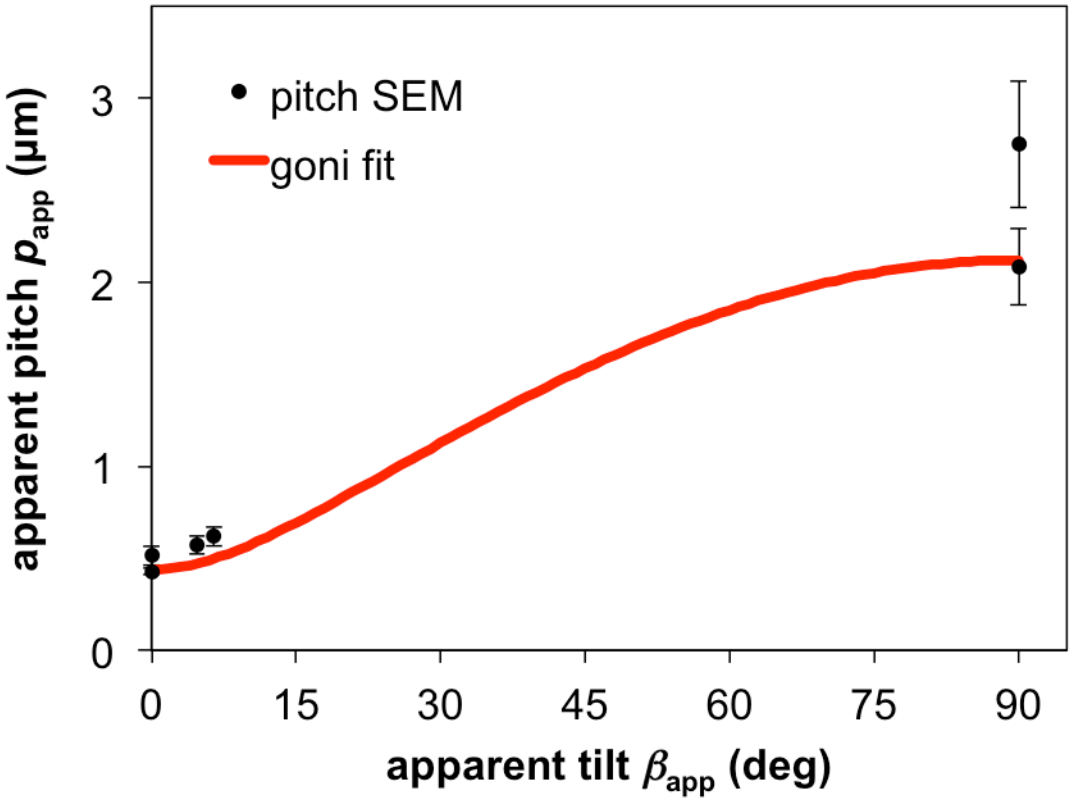

Figure S3. Reported apparent pitch values p_{app} measured in different directions of an SEM cross-section (sample m_{BTMSE}: m_{CNC} = 60:40), and compared with the angular pitch variation expected from our model and using α and p_{ka} obtained from the experimental goniometer data. The smallest apparent pitch p_{app} are consistent with the real pitch $p(\beta)$, while larger values are consistent with the artifact of domain misalignment.

2) Additional information on materials and methods

a) Sample preparation

Preparation of Cellulose Nanocrystals: CNC samples were provided by FPInnovations and were prepared using slightly different hydrolysis conditions from the cited reference.[1] For this specific batch, fully-bleached, commercial Kraft softwood pulp was first milled to pass through a 0.5 mm screen in a Wiley mill to ensure particle size uniformity and to increase surface area. Aliquots of concentrated sulphuric acid (95-98%) (Sigma-Aldrich) were diluted to 62 wt.% solutions. The milled pulp (60.0 g o.d.) was hydrolyzed in sulphuric acid (8.75mL of a sulphuric acid solution/g pulp) at a concentration of 62 wt.% and a temperature of 55 °C, respectively. The sulphuric acid solution was heated to the desired temperature (55 °C), added to the pulp in an Erlenmeyer flask in a hot water bath heated to the same temperature, and

allowed to hydrolyze the pulp under stirring with an impeller at high speed for 25 min. The cellulose suspension was then diluted with cold, deionized (DI) water (~10 times the volume of the acid solution used) to stop the hydrolysis, and allowed to settle overnight. The clear top layer was decanted off and the remaining white cloudy layer was centrifuged and washed twice with DI water. The suspension after the last centrifugation was then dialyzed against slow DI water using dialysis membrane tubes (12,000-14,000 molecular weight cut-off) until the water outside the dialysis membranes maintained at constant pH. After dialysis, the suspensions were diluted ~3 times with DI water owing to their high viscosity. Then, all suspensions were dispersed by subjecting them to ultrasound treatment using a VibraCell 750 Watts sonicator (Sonics & Materials, INC.) at 70% power for 30 minutes corresponding to an energy of ~ 9000 J/g. The sonicated suspensions were then filtered through a Whatman filter paper (#541 or #41) to remove any large particles. The purified suspensions were concentrated to the desired concentration using a rotavapor. The final CNC suspension was 3 wt.% and had a pH of 2.4.

Preparation of Organosilica/Cellulose nanocrystal (OS/CNC) Composite Films: Chiral nematic OS/CNC composite films were prepared by first sonicating the starting aqueous CNC suspension for 10 min. BTMSE was then added dropwise and the mixture was left to stir at room temperature for 1 h to obtain a homogeneous solution. The BTMSE/CNC mixtures were then cast into polystyrene Petri dishes (5 mL, Ø = 60 mm) and left to dry under ambient conditions (typically 18-24 h were required for complete drying). The different mass ratios of BTMSE:CNC used for the different chiral nematic composite samples are listed in Table 1. Chiral nematic CNC films were prepared using the same procedure but without the addition of BTMSE.

b) Sample characterization

Polarized optical microscopy (POM) was performed in reflection mode on a customized Zeiss Axio microscope using a halogen lamp (Zeiss HAL100) as a light source using Koehler illumination. Bright field (BF) images of the films were recorded with a 20× Epiplan Apochromat objective (NA = 0.6, WD = 1.7 mm) and a CCD camera (UI-3580LE-C-HQ, IDS). The reflected light was collected through a quarter-wave plate and a linear polarizing filter with adjustable mutual orientation to distinguish left- (LCP) and right-circularly polarized (RCP) light. The white balance reference was taken using a white Lambertian diffuser (USRS-99-010 AS-01158-060).

Spectroscopy: Reflection spectra were collected with a double-ended fiber (R200-7-SR, 00S-003413-01, Oceanoptics, placed in normal incidence with respect to the film surface) and analyzed with a spectrometer (AvaSpec-HS2048, Avantes), using a fiber-to-sample distance of 10 ± 0.5 mm and a white Lambertian diffuser as reference. White incident light was projected over a large surface (spot size Ø = 4.4 mm, area ~ 15 mm^2) in order to average out the variability of the local optical response.

Angular-resolved optical spectroscopy: Measurements were carried out using a lab-made goniometer: a xenon lamp (HPX-2000, Ocean Optics) was used as the light source and a spectrometer (AvaSpec-HS2048, Avantes) was used to analyze the scattered optical signal. The sample was mounted on a rotating stage in the center of the goniometer and illuminated with a collimated incident beam (light spot size Ø ~ 6 mm). A detector was mounted on an arm attached to a motorized rotation stage, and coupled the scattered light into an optic fiber connected to the spectrometer. The recorded light intensity was normalized with respect to a white Lambertian diffuser, while the exposure time was adjusted using an automatized high-dynamic-range (HDR) method.[2-4] Measurements were recorded at a fixed incident light angle θ_{in} = 30°, defined from the normal of the sample interface, and by scanning the scattered spectral intensity collected with the rotating detector.

Scanning Electron Microscopy (SEM) images were collected on a Leo Gemini 1530VP-Zeiss SEM. Samples were prepared by fracturing the films into small pieces and attaching them vertically to aluminum stubs so that the cross-section could be imaged. In order to prevent charging, the samples were attached using double-sided carbon adhesive tape and conductive silver paste, and coated with a thin layer of metal alloy using a sputter-coater (Emitech K550) with a Pd/Au target at a current of 55 mA for 6 s.

3) Comparison between pitch values from SEM and those predicted by the model.

The validity of our method and its accuracy can be assessed by comparing the estimated parameters with direct observations of film cross-sections in SEM. In **Figure 3b**, we report the pitch of the domains at zero tilt, $p(0) = \alpha\, p_{\mathrm{ka}}$, obtained either by goniometer analysis, by spectral analysis using the double-ended fiber in normal incidence, or by direct SEM observations of the film cross-sections, which are all in excellent agreement. The values we estimated for p_{ka} are expected to match with the pitch of domains tilted by 90°, which can also be compared to direct SEM observations. Indeed, cross-sections of polydomain films can occasionally capture the existence of these horizontal domains, and since vertical compression does not affect their horizontal periodicity, their pitch is expected to reflect the state of the suspension at the time of kinetic trapping, thus $p(90°) = p_{\mathrm{ka}}$ (**Figure S1**). As shown in **Figure 3c** for the sample where such a pattern is observed (m_{BTMSE}:m_{CNC} = 60:40), we have a good agreement with the value derived from goniometer analysis. This not only explains the apparent red-shift observed in off-specular conditions (**Figure 2c**), but also validates the robustness of our general approach.

4) Estimation of the OS and CNC volume fractions at the kinetic arrest.

a) Evaluation of mass and volume fractions in the final films

We control the mass of BTMSE and CNC combined and consider that in the final film all the BTMSE is fully condensed into OS. In order to evaluate the mass fraction c_{i} and volume

fraction Φ_i of CNC and OS in the final film, it is useful to consider a hypothetical intermediate (noted "itm") state where the film is completely dry but none of the BTMSE has yet initiated its condensation into OS. The mass fractions of BTMSE and CNC in that intermediate step are given by

$$c_{\mathrm{BTMSE}}^{\mathrm{itm}} = \mu/(1+\mu), \tag{S1}$$

$$c_{\mathrm{CNC}}^{\mathrm{itm}} = 1/(1+\mu), \tag{S2}$$

where $\mu = m_{\mathrm{BTMSE}}{:}\, m_{\mathrm{CNC}}$ is the mass ratio.

Their corresponding volume fractions are

$$\Phi_{\mathrm{BTMSE}}^{\mathrm{itm}} = \rho_{\mathrm{BTMSE}}^{-1} c_{\mathrm{BTMSE}}^{\mathrm{itm}} \Big/ \left(\rho_{\mathrm{CNC}}^{-1} c_{\mathrm{CNC}}^{\mathrm{itm}} + \rho_{\mathrm{BTMSE}}^{-1} c_{\mathrm{BTMSE}}^{\mathrm{itm}}\right), \tag{S3}$$

$$\Phi_{\mathrm{CNC}}^{\mathrm{itm}} = \rho_{\mathrm{CNC}}^{-1} c_{\mathrm{CNC}}^{\mathrm{itm}} \Big/ \left(\rho_{\mathrm{CNC}}^{-1} c_{\mathrm{CNC}}^{\mathrm{itm}} + \rho_{\mathrm{BTMSE}}^{-1} c_{\mathrm{BTMSE}}^{\mathrm{itm}}\right). \tag{S4}$$

In the final film, we assume then that all the BTMSE is condensed into OS. The mass fractions of CNC and OS in the final film can then be expressed as

$$c_{\mathrm{CNC}} = c_{\mathrm{CNC}}^{\mathrm{itm}} \Big/ \left(c_{\mathrm{CNC}}^{\mathrm{itm}} + c_{\mathrm{BTMSE}}^{\mathrm{itm}} M_{\mathrm{OS}}/M_{\mathrm{BTMSE}}\right), \tag{S5}$$

$$c_{\mathrm{OS}} = c_{\mathrm{BTMSE}}^{\mathrm{itm}} (M_{\mathrm{OS}}/M_{\mathrm{BTMSE}}) \Big/ \left(c_{\mathrm{CNC}}^{\mathrm{itm}} + c_{\mathrm{BTMSE}}^{\mathrm{itm}} M_{\mathrm{OS}}/M_{\mathrm{BTMSE}}\right). \tag{S6}$$

where M_{BTMSE} = 270.43 g mol^{-1} and M_{OS} = 132.22 g mol^{-1}.

The volume fractions in the film are then given by

$$\Phi_{\mathrm{CNC}} = \rho_{\mathrm{CNC}}^{-1} c_{\mathrm{CNC}} \Big/ \left(\rho_{\mathrm{CNC}}^{-1} c_{\mathrm{CNC}} + \rho_{\mathrm{OS}}^{-1} c_{\mathrm{OS}}\right), \tag{S7}$$

$$\Phi_{\mathrm{OS}} = \rho_{\mathrm{OS}}^{-1} c_{\mathrm{OS}} \Big/ \left(\rho_{\mathrm{CNC}}^{-1} c_{\mathrm{CNC}} + \rho_{\mathrm{OS}}^{-1} c_{\mathrm{OS}}\right), \tag{S8}$$

where we assumed the volumetric mass densities $\rho_{\mathrm{CNC}} = 1.600$ g cm^{-3}, $\rho_{\mathrm{BTMSE}} = 1.073$ g cm^{-3} and $\rho_{\mathrm{OS}} = 1.685$ g cm^{-3}, the latter being evaluated from the work of Wang et al. for non-porous OS.[6]

b) Volume fractions at the kinetic arrest

We introduce $\Phi_{\mathrm{CNC}}^{\mathrm{ka}}$ as the volume fraction of CNC at which the kinetic arrest occurs. From the onset of the kinetic arrest till the final formation of the film and the complete condensation

of BTMSE into OS, the volume of the sample decreases and thus the relative volume fraction of the CNCs increases from $\Phi_{\mathrm{CNC}}^{\mathrm{ka}}$ to Φ_{CNC}. If the volume loss is only due to a vertical compression, the ratio of the two volume fractions is given by

$$\Phi_{\mathrm{CNC}}^{\mathrm{ka}} = \alpha\, \Phi_{\mathrm{CNC}}, \tag{S9}$$

where α is the vertical scaling parameter that intervenes in our compression model.

This estimation is thus dependent on the hypothesis of pure vertical compression and to the accuracy of the determination of Φ_{CNC}, which relies on knowing the densities of the OS and CNC (both found in literature), their full condensation state (previous TGA measurements were consistent with that) and their respective mass fractions (known from masses of BTMSE and CNC used).

In order to estimate the concentration of OS species at the kinetic arrest, we first consider that no condensation has yet occurred at that point. The volume fraction of BTMSE (referred to as BTMSE* under such assumption) and water at the kinetic arrest can then be estimated as

$$\Phi_{\mathrm{BTMSE}^*}^{\mathrm{ka}} = \Phi_{\mathrm{CNC}}^{\mathrm{ka}} \left(\Phi_{\mathrm{BTMSE}}^{\mathrm{itm}}/\Phi_{\mathrm{CNC}}^{\mathrm{itm}}\right), \tag{S10}$$

$$\Phi_{\mathrm{water}^*}^{\mathrm{ka}} = 1 - \Phi_{\mathrm{BTMSE}^*}^{\mathrm{ka}} - \Phi_{\mathrm{CNC}}^{\mathrm{ka}}. \tag{S11}$$

The corresponding molar concentration of BTMSE is then given by

$$[\mathrm{BTMSE}^*]^{\mathrm{ka}} = \Phi_{\mathrm{BTMSE}^*}^{\mathrm{ka}}(\rho_{\mathrm{BTMSE}}/M_{\mathrm{BTMSE}}) \cdot 10^3 (\mathrm{cm}^3/\mathrm{L}). \tag{S12}$$

and its mass fraction as

$$c_{\mathrm{BTMSE}^*}^{\mathrm{ka}} = \rho_{\mathrm{BTMSE}}\, \Phi_{\mathrm{BTMSE}^*}^{\mathrm{ka}}/\rho_{\mathrm{ave}}^{\mathrm{ka}}, \tag{S13}$$

$$\rho_{\mathrm{ave}}^{\mathrm{ka}} = \rho_{\mathrm{BTMSE}}\, \Phi_{\mathrm{BTMSE}^*}^{\mathrm{ka}} + \rho_{\mathrm{CNC}}\, \Phi_{\mathrm{CNC}}^{\mathrm{ka}} + \rho_{\mathrm{water}}\, \Phi_{\mathrm{water}}^{\mathrm{ka}} \tag{S14}$$

where $\rho_{\mathrm{water}} = 1.000$ g cm^{-3}.

If instead we consider that all the BTMSE is condensed into OS when the kinetic arrest occurred, the volume fraction of OS at the kinetic arrest is then

$$\Phi_{\mathrm{OS}^{**}}^{\mathrm{ka}} = \Phi_{\mathrm{BTMSE}^*}^{\mathrm{ka}} \left(\frac{\rho_{\mathrm{BTMSE}}}{M_{\mathrm{BTMSE}}} \frac{M_{\mathrm{OS}}}{\rho_{\mathrm{OS}}}\right). \tag{S15}$$

As the full condensation of one BTMSE molecule releases six molecules of methanol, the suspension composition evolves from containing CNC, BTMSE and water to containing CNC, OS, water and methanol. However, both water and methanol evaporate and the exact ratio of methanol to water in the solvent at the point of kinetic arrest remains unknown. An upper limit for the concentration of methanol can still be estimated by assuming full condensation of OS and no evaporation of methanol at the moment of kinetic arrest:

$$[\mathrm{MeOH}^{**}]^{\mathrm{ka}} = 6[\mathrm{BTMSE}^{*}]^{\mathrm{ka}}, \tag{S16}$$

or in volume fraction in the sample, as

$$\Phi^{\mathrm{ka}}_{\mathrm{MeOH}^{**}} = [\mathrm{MeOH}^{**}]^{\mathrm{ka}}(M_{\mathrm{MeOH}}/\rho_{\mathrm{MeOH}}) \cdot 10^{-3}(\mathrm{L/cm^3}) , \tag{S17}$$

The volume fraction of water is then

$$\Phi^{\mathrm{ka}}_{\mathrm{water}^{**}} = 1 - \Phi^{\mathrm{ka}}_{\mathrm{CNC}} - \Phi^{\mathrm{ka}}_{\mathrm{OS}^{**}} - \Phi^{\mathrm{ka}}_{\mathrm{MeOH}^{**}}. \tag{S18}$$

Since the CNC and the OS do not contribute to the composition of the solvent, the volume fraction of methanol in the solvent is then given by:

$$\Phi^{\mathrm{ka,solv}}_{\mathrm{MeOH}^{**}} = \Phi^{\mathrm{ka}}_{\mathrm{MeOH}^{**}} / \left(\Phi^{\mathrm{ka}}_{\mathrm{MeOH}^{**}} + \Phi^{\mathrm{ka}}_{\mathrm{water}^{**}}\right). \tag{S19}$$

$$[\mathrm{MeOH}^{**}]^{\mathrm{ka,solv}} = [\mathrm{MeOH}^{**}]^{\mathrm{ka}} / \left(\Phi^{\mathrm{ka}}_{\mathrm{MeOH}^{**}} + \Phi^{\mathrm{ka}}_{\mathrm{water}^{**}}\right). \tag{S20}$$

The upper limit of this evaluation is the pure methanol, namely $\Phi^{\mathrm{ka,solv}}_{\mathrm{MeOH}^{**}} \leq 1$ and $[\mathrm{MeOH}^{**}]^{\mathrm{ka,solv}} \leq (\rho_{\mathrm{MeOH}}/M_{\mathrm{MeOH}}) \cdot 10^{3}(\mathrm{cm^3/L}) = 24.7$ M.

A value larger than this is unphysical and justifies applying an upper limit to $[\mathrm{MeOH}^{**}]^{\mathrm{ka,solv}} \leq 24.7$ M.

The solvent relative permittivity is then evaluated as

$$\varepsilon_{\mathrm{r}}^{**,\mathrm{ka}} = \Phi^{\mathrm{ka,solv}}_{\mathrm{MeOH}^{**}} \varepsilon_{\mathrm{r,MeOH}} + (1 - \Phi^{\mathrm{ka,solv}}_{\mathrm{MeOH}^{**}}) \varepsilon_{\mathrm{r,water}}. \tag{S21}$$

where $\varepsilon_{\mathrm{r,MeOH}} = 32.7$ and $\varepsilon_{\mathrm{r,water}} = 78.4$.

A visual illustration of the different calculations is provided in Figures S4-S8, for an increasing amount of BTMSE added. The bars are topped by the source of the information,

namely "goni" stands for goniometer (i.e., angular-resolved optical spectroscopy) and (S#) corresponds to the equations S# used, as provided in these Supporting Information.

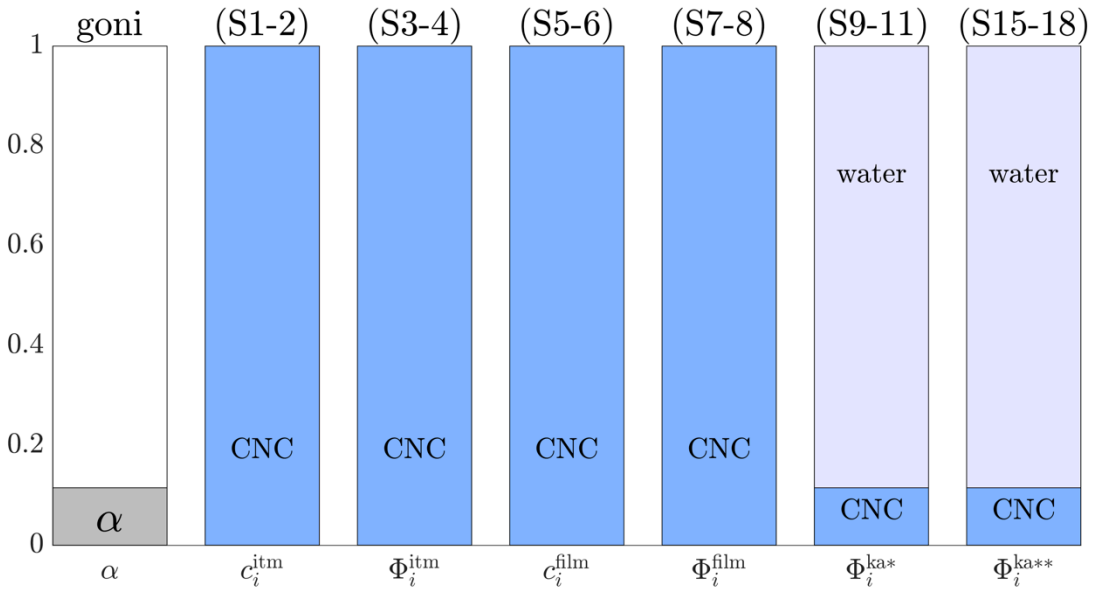

Figure S4. Visualization of the data processing for the sample m_{BTMSE}: m_{CNC} = 0:100.

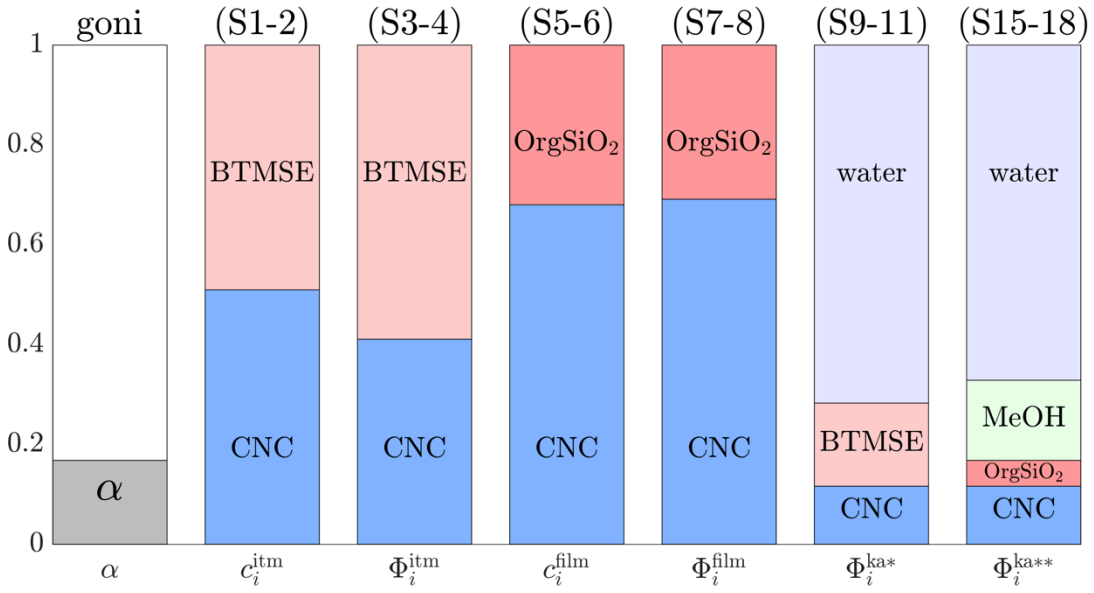

Figure S5. Visualization of the data processing for the sample m_{BTMSE}: m_{CNC} = 49:51.

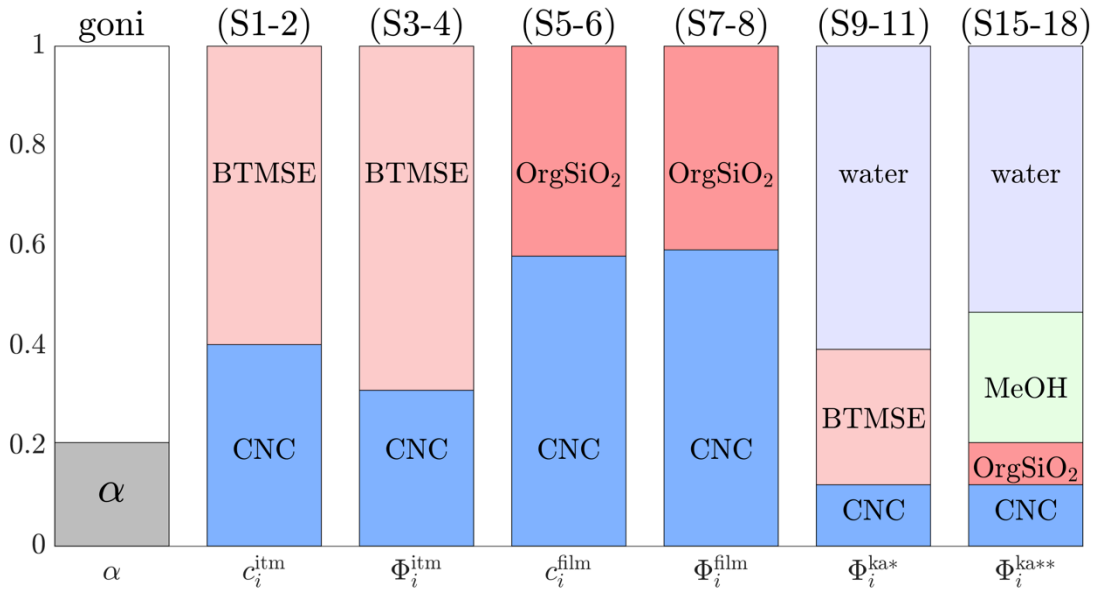

Figure S6. Visualization of the data processing for the sample m_{BTMSE}: m_{CNC} = 40:60.

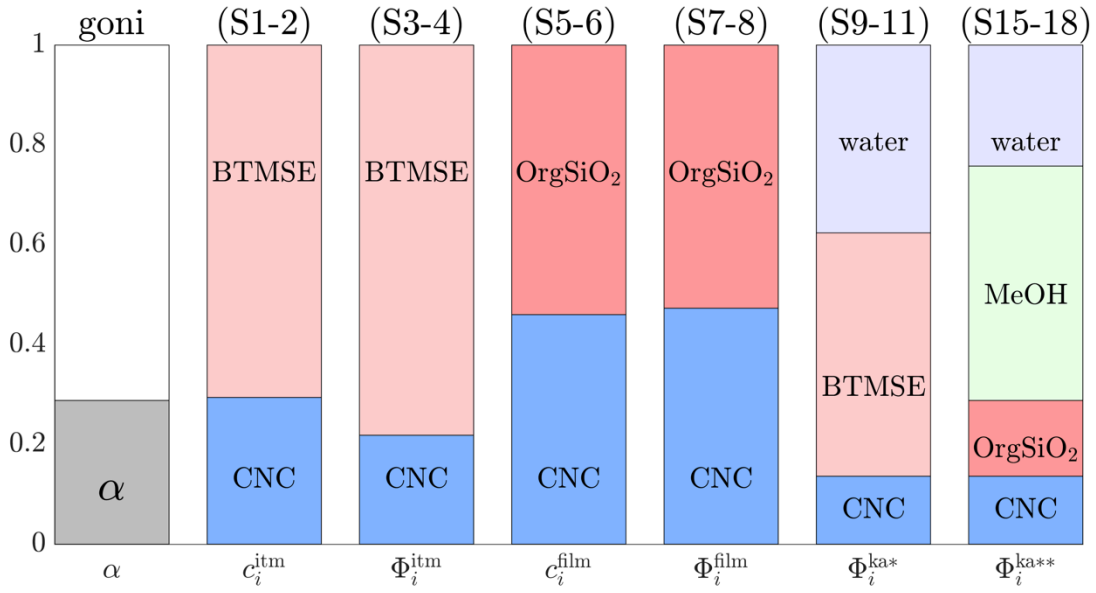

Figure S7. Visualization of the data processing for the sample m_{BTMSE}: m_{CNC} = 71:29.

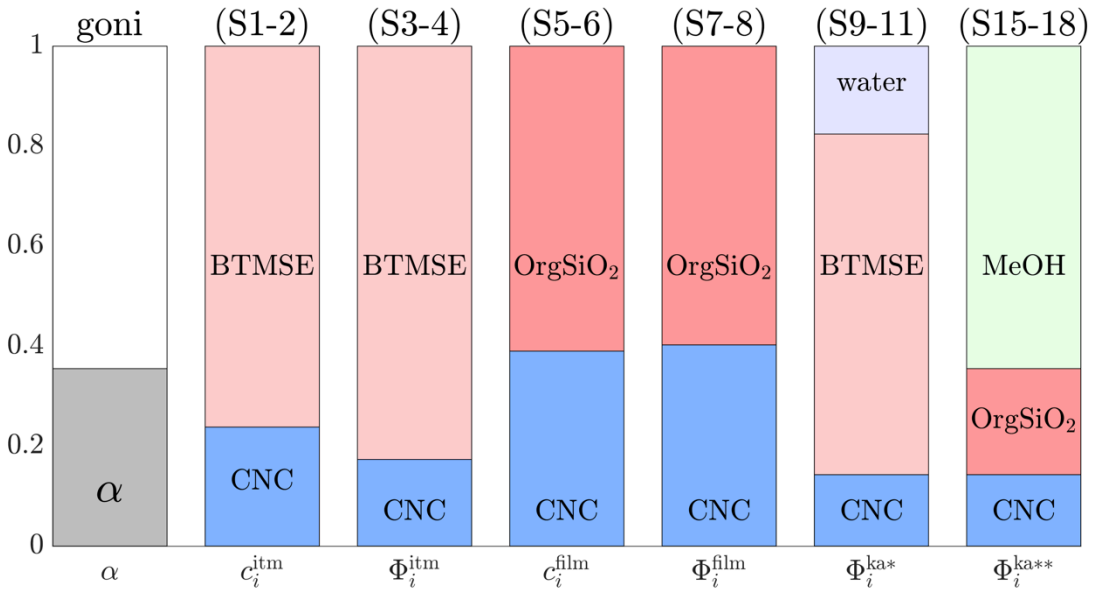

Figure S8. Visualization of the data processing for the sample m_{BTMSE}: m_{CNC} = 76:24.

c) Average optical index of OS/CNC films

The average optical index of the films were estimated as following:

$$n_{\mathrm{ave}}^{\mathrm{film}} = \sqrt{n_{\mathrm{CNC}}^2 \Phi_{\mathrm{CNC}} + n_{\mathrm{OS}}^2 \Phi_{\mathrm{OS}}} \qquad \text{(S22)}$$

with n_{CNC} = 1.555 (from ref.[5]) and n_{OS} = 1.510.[6]

5) References

[1] W. Y. Hamad, T. Q. Hu, *Can. J. Chem. Eng.* **2010**, *88*, 392.

[2] B. Frka-Petesic, G. Guidetti, G. Kamita, S. Vignolini, *Adv. Mater.* **2017**, *29*, 1701469.

[3] G. Kamita, B. Frka-Petesic, A. Allard, M. Dargaud, K. King, A. G. A. G. Dumanli, S. Vignolini, *Adv. Opt. Mater.* **2016**, *4*, 1950.

[4] D.-P. Song, G. Jacucci, F. Dundar, A. Naik, H.-F. Fei, S. Vignolini, J. J. Watkins, *Macromolecules* **2018**, *51*, 2395.

[5] A. G. Dumanli, H. M. van der Kooij, G. Kamita, E. Reisner, J. J. Baumberg, U. Steiner, S. Vignolini, *ACS Appl. Mater. Interfaces* **2014**, *6*, 12302.

[6] W. Wang, D. Grozea, S. Kohli, D. D. Perovic, G. A. Ozin, *ACS Nano* **2011**, *5*, 1267.